

Supporting Information

Dipole-Mediated Exciton Management Strategy Enabled by Reticular Chemistry

Ruomeng Wan^a, Dong-Gwang Ha^a, Jin-Hu Dou^a, Woo Seok Lee^b, Tianyang Chen^a, Julius J. Oppenheim^a, Jian Li^c, William A. Tisdale^{b*}, Mircea Dincă^{a*}

a. Department of Chemistry, Massachusetts Institute of Technology, Cambridge 02138, Massachusetts, USA

b. Department of Chemical Engineering, Massachusetts Institute of Technology, Cambridge 02128, Massachusetts, USA

c. Department of Materials and Environmental Chemistry, Stockholm University, Stockholm, Sweden

Table of Contents

Section 1. Materials and Synthesis	p2
Section 2. Experimental Methods	p3
Section 3. Synchrotron PXRD Analysis	p5
Section 4. HR-TEM Measurement Parameters and Analysis	p6
Section 5. Electron Diffraction Analysis	p7
Section 6. Energy Levels and Spectral Overlap	p8
Section 7. Time-resolved Photoluminescence Experimental Details and Spectra	p10
Section 8. Photoluminescence Quantum Yield Raw Data and Discussion	p16
Section 9. TD-DFT Calculations	p19
Section 10. References	p22

Section 1. Materials and Synthesis

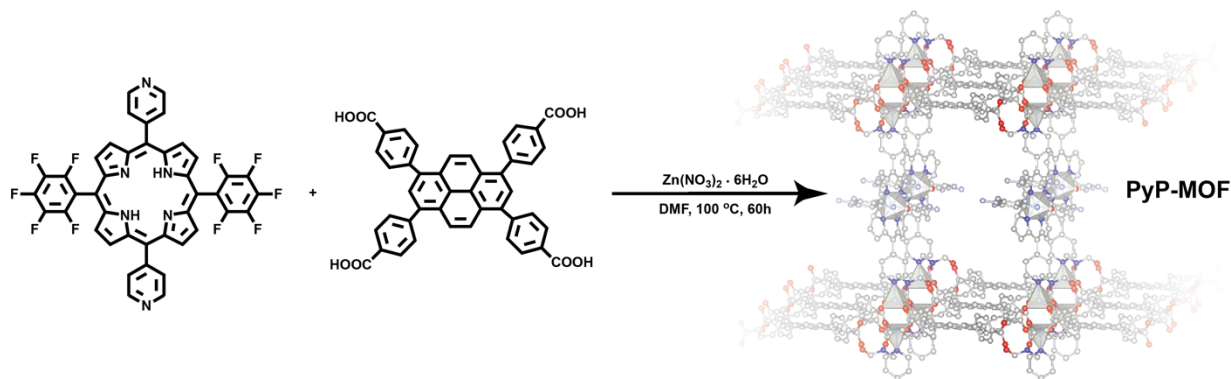
1.1 Materials

Zn(NO₃)₂·6H₂O (Avantor Performance Materials, Inc.), and N,N-dimethylformamide (DMF, 99.9%, EMD Millipore) were obtained from commercial sources and used as received. (5,15-dipyridyl-10,20-bis(pentafluorophenyl)) porphyrin (**H₂P**), and 4,4',4'',4'''-(pyrene-1,3,6,8-tetrayl) tetra-benzoic acid (**H₄TBAPy**) are prepared according to literature procedures.^{1,2}

1.2 Synthesis

Preparation of PyP-MOF The following solvothermal condition for the growth of **PyP-MOF** was adapted from synthetic procedures of structurally analogous paddlewheel pillared MOFs reported in literature.¹ 5,15-dipyridyl-10,20-bis(pentafluorophenyl) porphyrin (**H₂P**) (8.0 mg, 0.01 mmol), **H₄TBAPy** (13.7 mg, 0.02 mmol), and Zn(NO₃)₂·6H₂O (6.5 mg, 0.02 mmol) were dissolved in DMF (5 mL). The mixture was sonicated for 20 min, and the resulting solution was loaded into a Teflon-lined screw-cap vial. The solution mixture was then heated in an oven at 100 °C for 60 h. After gradually cooling to room temperature over 12h, red crystals of **PyP-MOF** were obtained. Centrifugation of the mixture allowed separation of the crystals, which were thoroughly washed with DMF and acetone (3 times each, soaked for 1h between the washes). The washes were performed until no more residual ligands were seen in the supernatant of the washes. The resulting crystals were dried overnight to yield 12.8 mg of **PyP-MOF**. Elemental analysis: Calcd. for **PyP-MOF**: (%) C, 61.87; H, 2.30; N, 5.04. Calcd. for **PyP-MOF**·DMF·5H₂O: (%) C, 58.33; H, 3.03; N, 5.35 Found: C, 57.55; H, 3.32; N, 5.51.

Scheme S1. Synthetic pathway for **PyP-MOF**.



Section 2. Experimental Methods

2.1 (Cryo) HR-TEM and Electron Diffraction

(Cryo) HR-TEM and electron diffraction of **PyP-MOF** (**Figure 3**, **Figure 4** and **Figure S1**) were obtained with a Talos Arctica G2 transmission electron microscope operated at an accelerating voltage of 200 kV with Falcon3EC direct electron detector and a Ceta 16M Camera, respectively. Samples were prepared by sonicating **PyP-MOF** (~2 mg) crystals in methanol (~2 mL) for 5s. The suspension was then loaded onto C-flat Cu TEM grids with holey carbon film via drop-casting. The HR-TEM measurement conditions were adapted from previous report.³ The TEM dose rate was at 35.60 e/Å². All image acquisition was done using EPU at an exposure time of 1.40 s, with focusing done adjacent to the region imaged to minimize beam exposure prior to image acquisition (standard low dose imaging protocols). Analysis of the raw HR-TEM data was done using Gatan Microscopy Suite software (GMS 3).

2.2 Synchrotron Powder X-ray Diffraction (PXRD)

High-resolution synchrotron PXRD data were obtained at beamline 11-BM of the Advanced Photon Source (APS), Argonne National Laboratory, using the Debye-Scherrer geometry and an average wavelength of 0.458164 Å. Data collection were performed at 100 K. Discrete detectors covering an angular range from -6 to 28° 2θ are scanned over a 34° 2θ range, with data points collected every 0.001° 2θ (actual 2θ/step is 0.0009984375°) and scan speed of 0.1 s/step. The 11-BM instrument uses X-ray optics with two platinum-stripped mirrors and a double-crystal Si (111) monochromator, where the second crystal has an adjustable sagittal bend.⁴ Ion chambers monitor incident flux. A vertical Huber 480 goniometer, equipped with a Heidenhain encoder, positions an analyzer system comprised of twelve perfect Si (111) analyzers and twelve Oxford-Danfysik LaCl₃ scintillators, with a spacing of 2° 2θ.⁵ Analyzer orientation can be adjusted individually on two axes. A three-axis translation stage holds the sample mounting and allows it to be spun, typically at ~5400 RPM (90 Hz). A Mitsubishi robotic arm is used to mount and dismount samples on the diffractometer.⁶ Oxford Cryosystems Cryostream Plus device allows sample temperatures to be controlled over the range 80-500 K when the robot is used. The diffractometer is controlled via EPICS.⁷ Data are collected while continually scanning the diffractometer 2θ arm. A mixture of NIST standard reference materials, Si (SRM 640c) and Al₂O₃ (SRM 676) is used to calibrate the instrument, where the Si lattice constant determines the wavelength for each detector. Corrections are applied for detector sensitivity, 2θ offset, small differences in wavelength between detectors, and the source intensity, as noted by the ion chamber before merging the data into a single set of intensities evenly spaced in 2θ.

2.3 Elemental Analysis

Elemental analysis was performed by Robertson Microlit Laboratories, Ledgewood, New Jersey.

2.4 Diffuse Reflectance UV-Vis

Diffuse reflectance UV-Vis spectra (DRUV-Vis) between 200 nm and 800 nm were collected on a Cary 5000i spectrophotometer, fitted with a PIKE technologies UV-Vis DiffusIR accessory. A scan rate of 200 nm/min was applied under ambient conditions. The samples were prepared by grinding powders with KBr using a mortar and a pestle to 1 wt% dilution. A KBr baseline and a zero-background correction were collected prior to the sample measurements, and the spectra were normalized to a 100% KBr baseline. The Kubelka–Munk equation $F(R) = (1 - R)^2/2R$ was applied, and the Kubelka–Munk function transformed spectra were then normalized.

2.5 Time-resolved Photoluminescence (PL)

Instrumental Set-up Time-resolved PL was measured with a streak camera (HAMAMATSU Streak Scope C10627 attached to HAMAMATSU Digital Camera C9300, coupled with Hamamatsu synchronous delay generator C10647 and HAMAMATSU power supply unit C10627). The samples were excited with a $\lambda = 371$ HAMAMATSU picosecond light pulser C10196, set to a repetition rate of 1.7 MHz (Trigger Division=1).

Measurement Conditions Time-resolved PL data for different samples were recorded using approximately constant excitation pulse energy of 20 μ W. The laser spot size is measured to be approximately 0.07 cm², corresponding to a power flux fluence of \sim 0.29 mW/cm². All measurements were performed using quartz substrate under ambient conditions. The substrates were cleaned by sonicating in acetone for 2 min (two times), followed by soaking in boiling isopropanol for 2 min (two times).

Data Collection and Analysis Streak camera measurements were performed using High Performance Digital Temporal Analyzer (TPD-TA) Ver. 9.4. The raw time-resolved PL data were background-corrected, and the maximum detected value was normalized to 1.

Sample Preparation For detailed sample preparation method corresponding to each experiment, please see **ESI Section 7**.

2.6 PL Quantum Yield

The measurements of PL quantum yield (QY) were performed using the absolute quantum yield method in an integrating sphere.⁸ The excitation light from a 405 nm laser diode (Picoquant, LDHDC-405M, continuous wave mode) was directed into an integrating sphere (Labsphere) that housed a DMF suspension of **PyP-MOF**. The output signal was collected by an optical fiber mounted on an exit port of the integrating sphere and was directed into a spectrograph (Princeton Instruments, SP-2500) mounted with a cooled charge-coupled detector (Princeton Instruments, Pixis). Neutral density and color glass filters were inserted in front of the spectrograph to avoid saturating the detector's pixels because of the large difference in the excitation and the emission signals' magnitudes.

Section 3. Synchrotron PXRD Analysis

Table S1. Unit cell information obtained from Pawley refinement of synchrotron PXRD data, and the Pawley refinement details.

Synchrotron PXRD Data Analysis			
Unit Cell and Symmetry	Lattice Parameters		
Monoclinic Centered Space Group C12/m1	$a = 22.8094(2)$ $b = 21.8663(5)$ $c = 21.8204(6)$	$\alpha = 90.0$ $\beta = 95.6985(3)$ $\gamma = 90.0$	Volume 10829.35(7)
Pawley Refinement Details $R_{wp} = 5.19 \%$ $R_{exp} = 3.66 \%$ $gof = 1.42$	<p>The figure is a plot of synchrotron PXRD data. The x-axis is labeled 'Q (Å⁻¹)' and ranges from 0.4 to 2.0. The y-axis represents intensity in counts, with a scale bar indicating 1 × 10⁴ counts. Three data series are shown: 'Experimental' (blue line), 'Simulated' (red line), and 'Difference' (grey line). The experimental and simulated curves show a series of peaks, with the most prominent peak at approximately Q = 0.45. The difference curve shows a small peak at the same position, indicating a slight mismatch between the experimental data and the simulated model.</p>		

Section 4. HR-TEM Measurement Parameters and Analysis

Table S2. Summary of data collection parameters for HRTEM.

Cryo-HRTEM Data Collection Parameters Summary	
Microscope / Detector	Talos Arctica G2 / Falcon 3EC
Extraction voltage	4100 V
Acceleration voltage	200 kV
Gun lens	4
Spot size (C1)	2
Intensity (C2)	45.383%
Parallel illumination	Yes
Condenser aperture	30 μm
Objective lens spherical aberration (Cs)	2.7 mm
Nominal magnification	190,000X
Nominal pixel size	0.7656 \AA
Dose rate on camera	14.90 el/px/s
Exposure time	1.40 s
Total exposure on specimen	35.60 el/ \AA^2
Fractions	11 (55 frames aligned)
Nominal defocus range (min, max, step)	-0.2

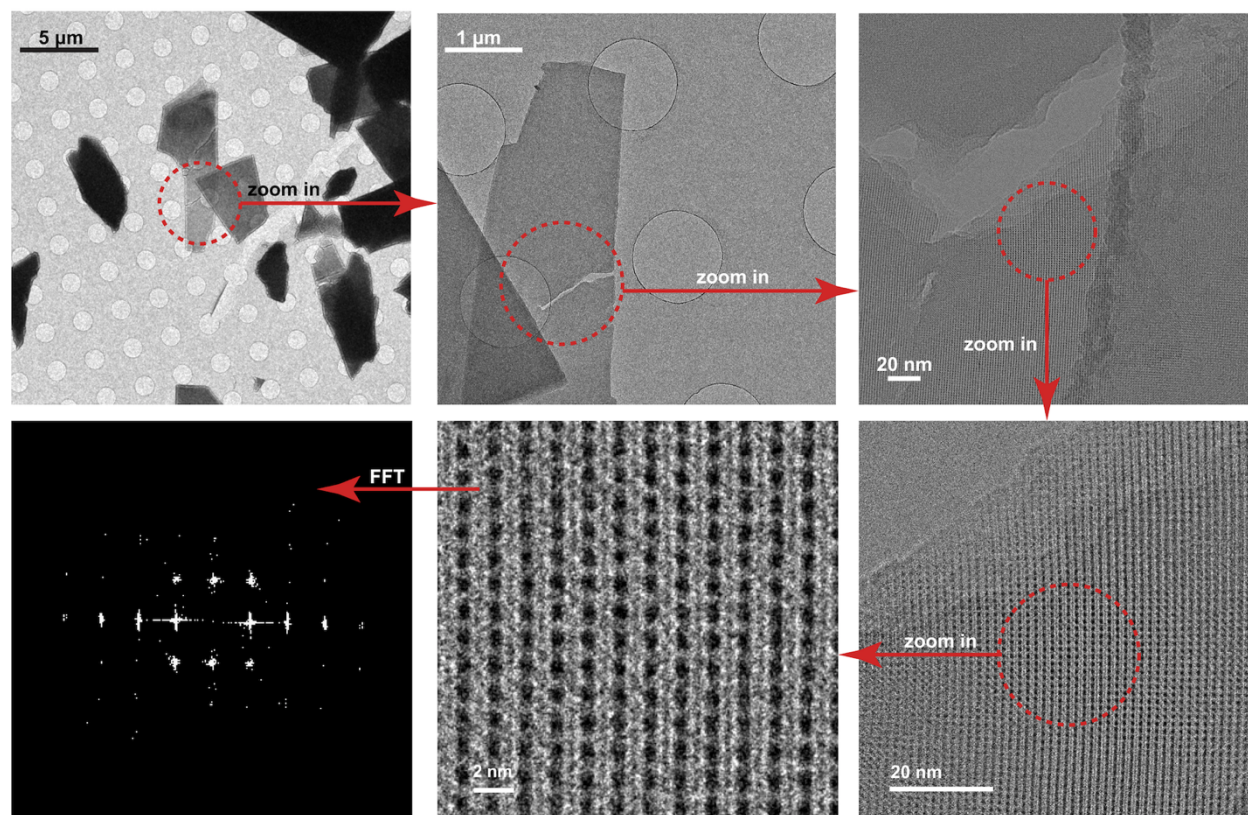


Figure S1. (Cryo) HR-TEM data collection process from low magnification to high magnification, followed by fast Fourier transform (FFT) analysis.

Section 5. Electron Diffraction Analysis

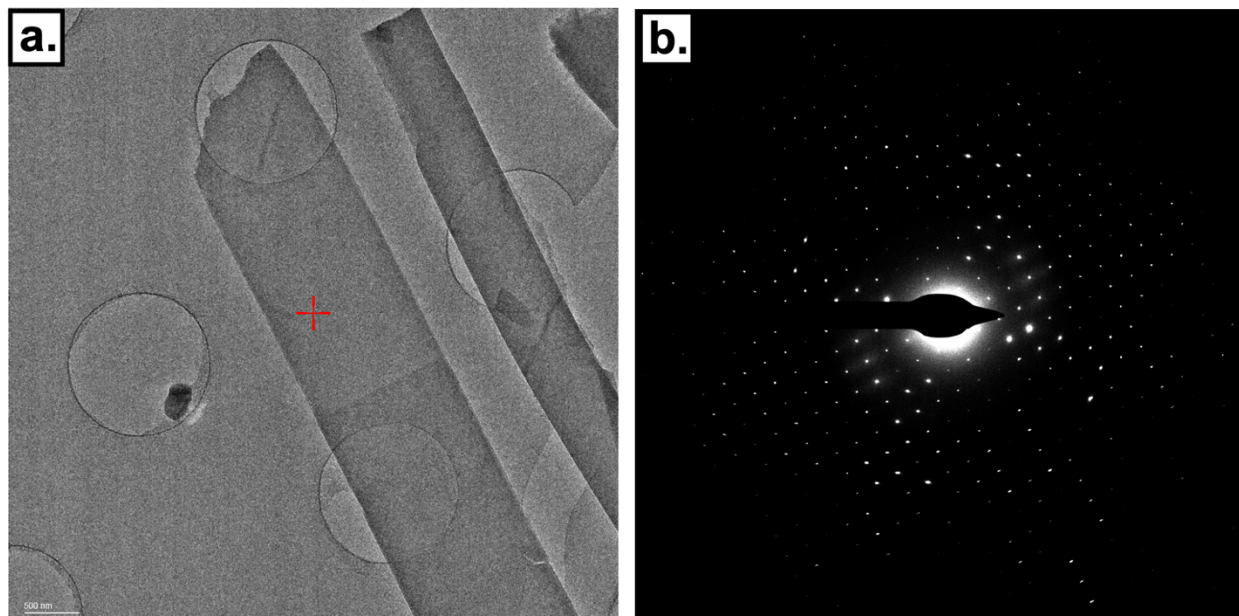


Figure S2. Electron diffraction pattern obtained with the incident electron beam along the pillaring direction (b), and the corresponding diffraction spot where the electron beam was focused (a).

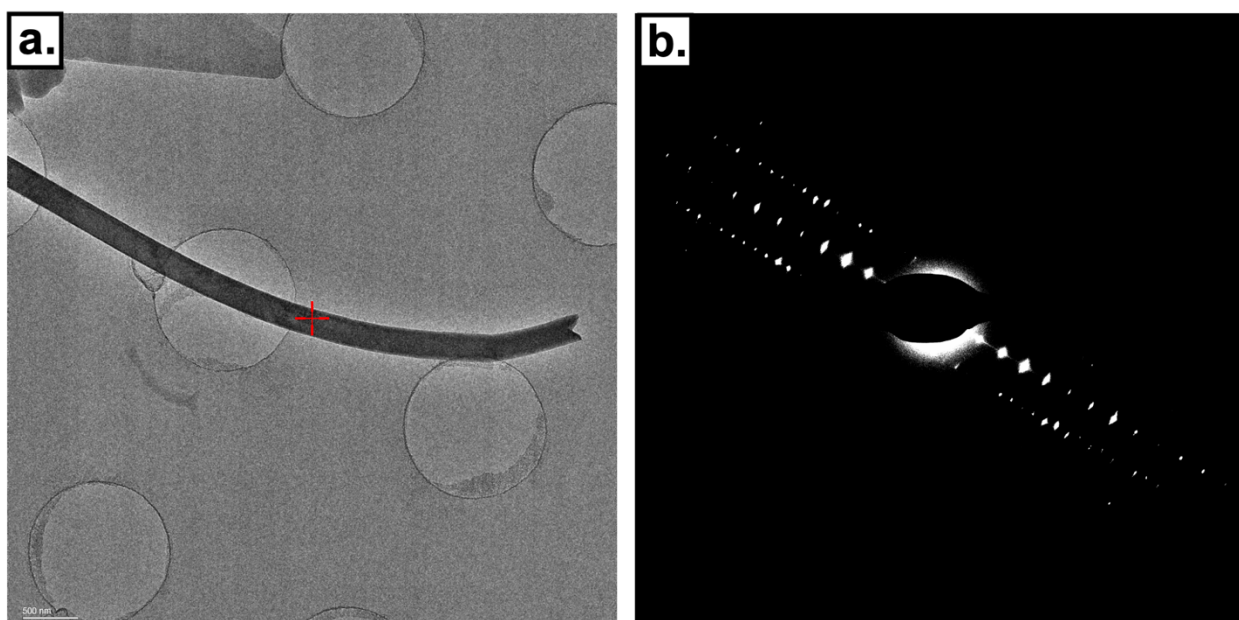


Figure S3. Electron diffraction pattern obtained with the incident electron beam perpendicular to the pillaring direction (b), and the corresponding diffraction spot where the electron beam was focused (a).

Section 6. Energy Levels and Spectral Overlap

6.1 Summary of Diffuse Reflectance UV-Vis Absorption Spectra

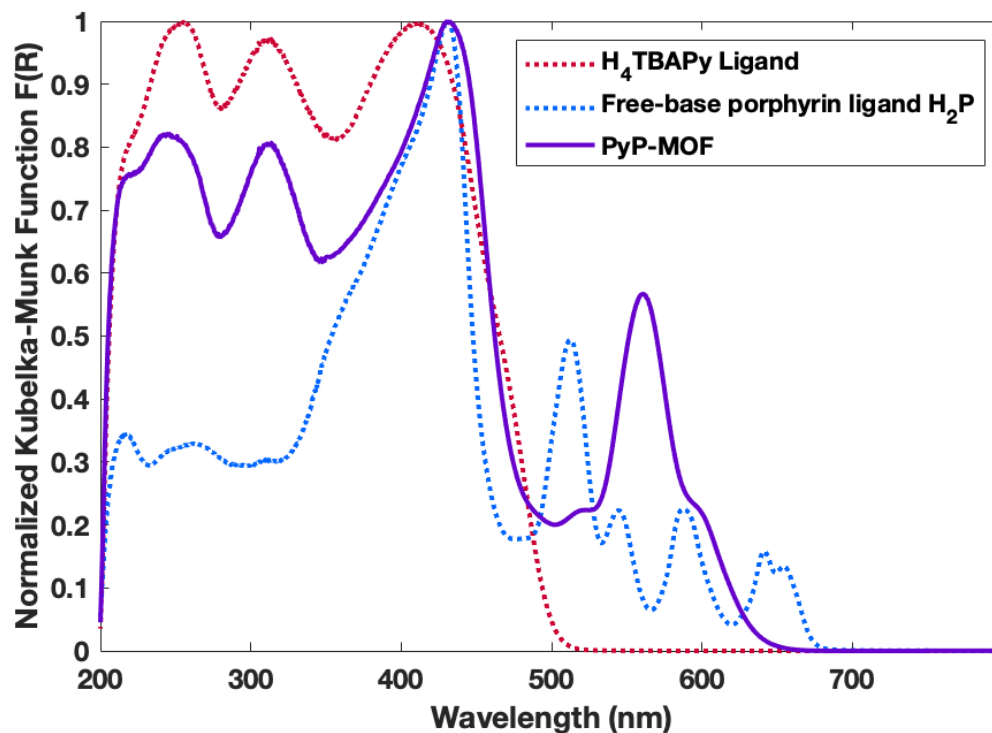


Figure S4. Diffuse reflectance UV-Vis spectra of PyP-MOF and its building blocks (H_4TBAPy and H_2P). All samples were diluted in KBr to 1 wt%.

6.2 Discussion on the Comparison Between H_2P and $\text{Zn}^{\text{II}}\text{-P}$ Absorption Energy Levels

Upon incorporation into the PyP-MOF, the free-base porphyrin ligand H_2P is metalated to form a Zn^{II} -porphyrin moiety. This increases the symmetry of the porphyrin moiety from D_{2h} point group to D_{4h} point group. The observed change in the number of peaks in the Q-band region upon metalation (**Figure S5**) is consistent with group theory analysis of porphyrin spectra, which has been investigated in detail in literature.⁹

The comparison between the absorption spectra of H_2P with that of $\text{Zn}^{\text{II}}\text{-P}$ also provides justification of our choice of applying H_2P ligand instead of $\text{Zn}^{\text{II}}\text{-P}$ in the control experiment. In this specific case, H_2P can serve as a valid alternative for $\text{Zn}^{\text{II}}\text{-P}$ due to their conversed HOMO/LUMO energy levels. The influence of metalation on porphyrin energy level has been categorized based on the metal center's d -electron count. Closed-shell d^{10} metalloporphyrin belongs to a special category where metalation neither blue-shifts nor red-shifts the $\pi \rightarrow \pi^*$ absorption energy. This is because the closed-shell d -orbitals lie too low in energy to mix with either the HOMO (π) or the LUMO (π^*). For more detailed discussion regarding this topic, please reference the well-established work by Gouterman.⁹

Since Zn^{II} falls into this special category of d^{10} metalloporphyrin, we observed that Zn^{II} -P and H_2P share the same absorption energy, as shown in **Figure S5** below. Based on both the theoretical foundation⁹ and experimental evidence, we rationalized that for the specific purpose of our control experiment (where only the energy level is of concern), the free-base porphyrin can serve as a valid option.

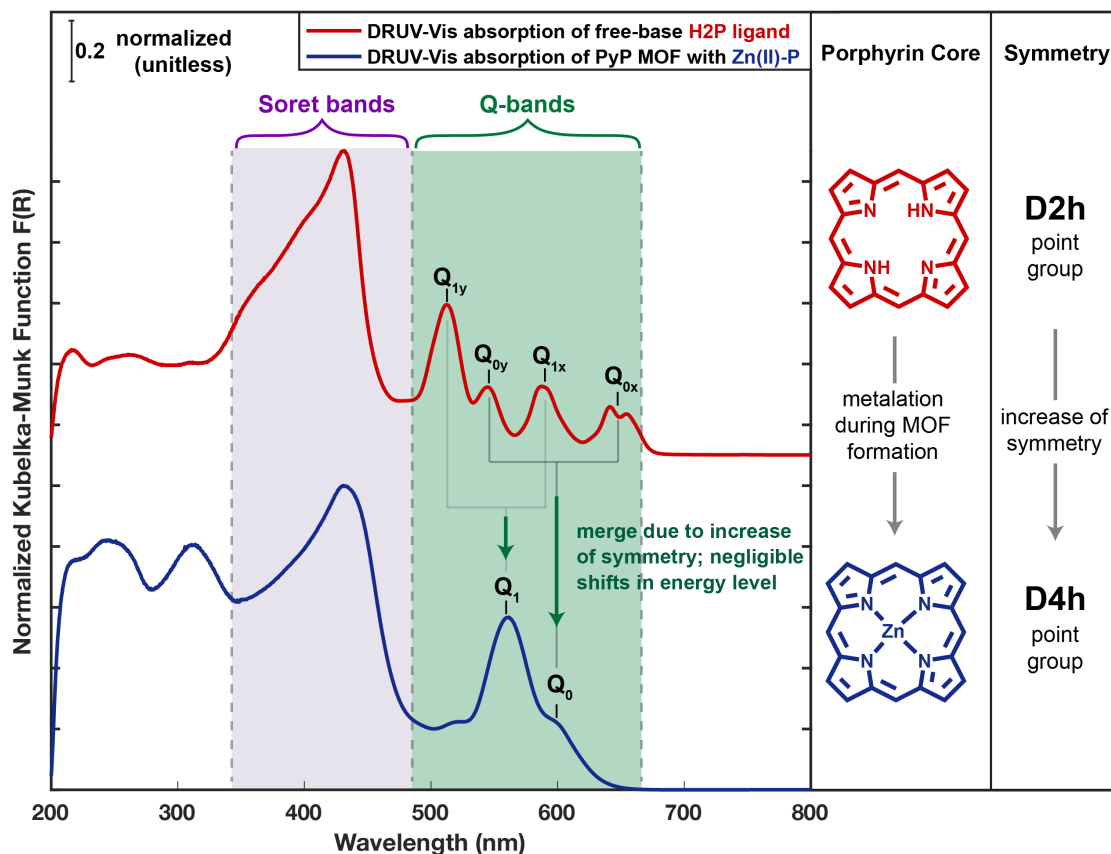


Figure S5. Comparison between the DRUV-Vis absorption spectra of the porphyrin moiety before and after incorporation into the **PyP-MOF**. The porphyrin moiety undergoes metalation upon incorporation into the **PyP-MOF**, forming Zn^{II} -P from free-base H_2P . The metalation is accompanied by an increase in symmetry, which is consistent with the reduced number of Q-bands from 4 peaks to 2 peaks. It is also worth noting that for the special case of Zn^{II} (d^{10}) metalloporphyrin, metalation does not shift the absorption ($\pi \rightarrow \pi^*$ transition) energy level. Since only the energy level (not the symmetry) is relevant for the control experiment, both the free-base and the Zn^{II} porphyrins are valid options to be used for this particular purpose.

6.3. Spectral Overlap Between the Donor and the Acceptor

The control experiment directly demonstrates that the spectral overlap between the donor and the acceptor is sufficient for allowing efficient energy transfer. This is further corroborated by the spectral overlap observed from overlapping the donor emission spectra and the acceptor absorption profile (**Figure S6**).

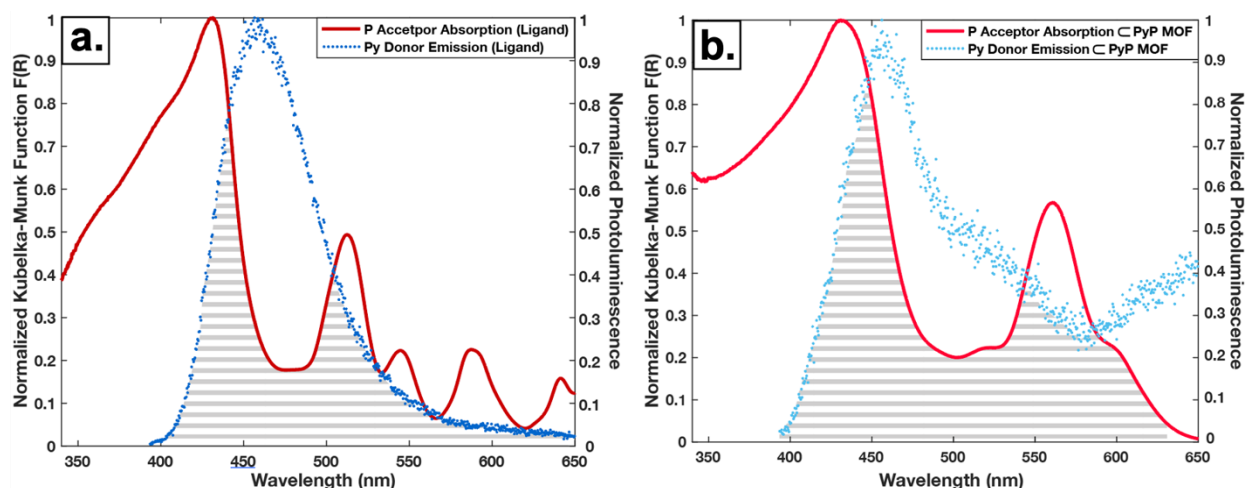


Figure S6. Comparison of the donor (Py) emission spectra and acceptor (P) absorption spectra for the D-A pair before (a) and after (b) incorporation into PyP-MOF structure.

Section 7. Time-resolved Photoluminescence Experimental Details and Spectra

7.1 H₄TBAPy Ligand (Diluted in Polystyrene)

Sample preparation

2 mg H₄TBAPy ligand and 200 mg polystyrene were dissolved in 4 mL DMF, and the mixture was sonicated until the solids complete dissolved. The mixture was then spin-coated onto clean quartz substrates at a spin speed of 500 RPM for 5s followed by 2000 RPM for 45s.

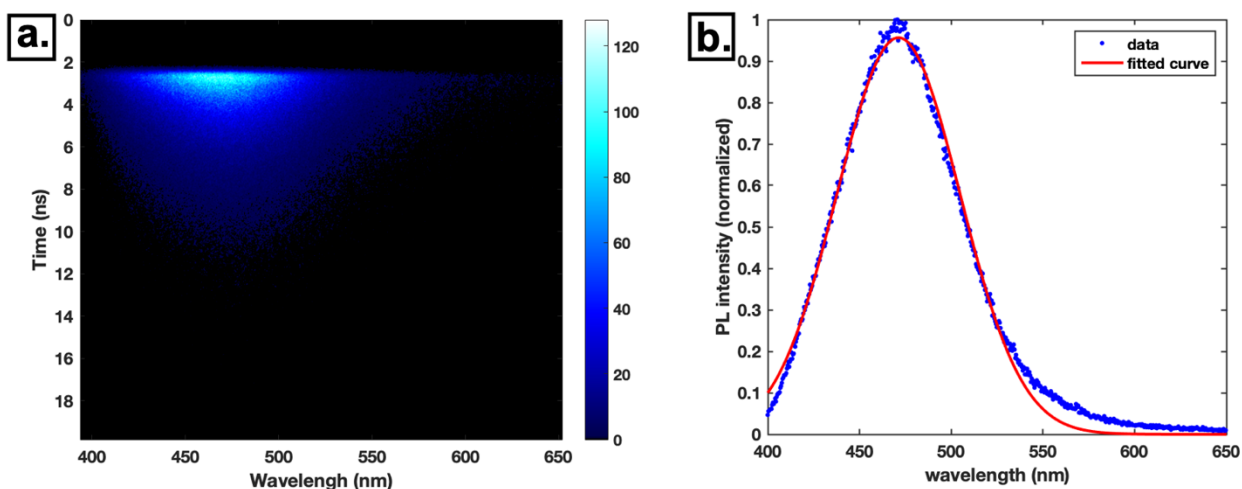


Figure S7. (a) Time-resolved spectrally resolved photoluminescence trace of H₄TBAPy (diluted solid-state sample in polystyrene). (b) Photoluminescence of H₄TBAPy integrated over time (0-20 ns).

Concentration-dependent Studies

A series of concentration dependent studies on the exciton decay life of **H₄TBAPy** was performed, using **H₄TBAPy** diluted in polystyrene matrix to different concentrations. Specifically, 2 mg, 4 mg, 8 mg and 16 mg were dissolved in 4 mL DMF with 200 mg polystyrene. Each sample was sonicated till both **H₄TBAPy** and polystyrene completely dissolved, yielding transparent solutions. The solutions correspond to four different concentrations of 1 wt%, 2 wt%, 4 wt% and 8 wt%, respectively. These solutions were then spin-coated onto clean quartz substrates at a spin speed of 500 RPM for 5s followed by 2000 RPM for 45s (please see **ESI Section 2.5** for substrate cleaning procedures).

Transient PL measurement was performed on each of the sample following the conditions detailed in **ESI Section 2.5**. The time-integrated spectra and the decay curves of the samples of different concentrations were compared, yielding the following results:

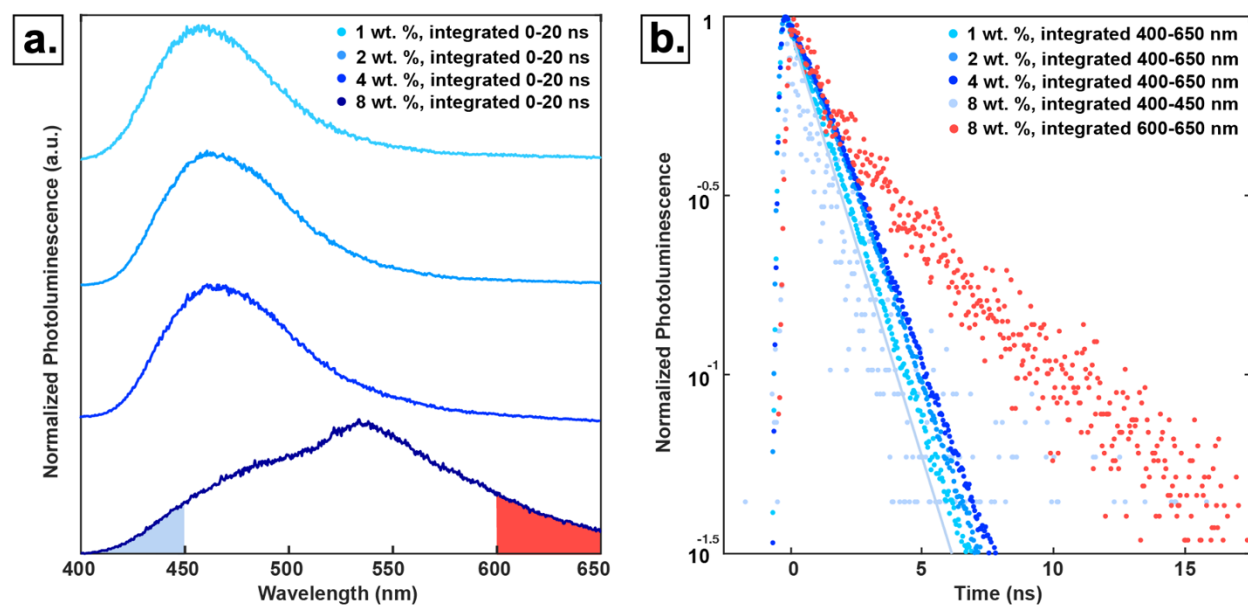


Figure S8. (a) Integrated PL (normalized) of **H₄TBAPy** incorporated in polystyrene matrix at concentrations of 1 wt%, 2 wt%, 4 wt% and 8 wt%. The PL data are integrated from 0 to 20 ns. **(b)** The PL decay curve of **H₄TBAPy** incorporated in polystyrene matrix at concentrations of 1 wt%, 2 wt%, 4 wt% and 8 wt%. The samples at concentrations of 1 wt%, 2 wt% and 4 wt% are integrated over the entire spectral range of 400 nm to 650 nm. Since the sample at concentration of 8 wt% involves contribution of multiple species, the integration was performed 400 nm-450 nm and 600 nm-650 nm in an attempt to separate the contribution from the monomer and the excimer, respectively.

As shown in **Figure S8**, over the concentration range of 1 wt% to 4 wt%, the PL from **H₄TBAPy** diluted in polystyrene matrix is dominated by the monomer emission, which is centered around 460 nm, with a lifetime of approximately 1.8 ns. Upon further doubling the concentration to 8 wt%, significant contribution from excimer species can be observed, as evidenced by a broad red-shifted peak growing in (**Figure S8a, bottom**). In an attempt to separate the contributions from the

monomer and excimer species for lifetime calculation, the integration was performed over the blue-end (400 nm-450 nm) and the red-end (600 nm-650 nm) of the spectral range, respectively. The integration over 400nm to 450 nm yielded a lifetime consistent with the monomer emission (~ 1.8 ns), while the integration over 600 nm to 650 nm yielded a much longer lifetime of ~ 4 ns, consistent with the typical decay of excimer species.

7.2 PyP-MOF

Sample preparation

(i) **Diluted in polymer matrix**

2 mg PyP-MOF and 200 mg polystyrene were suspended in 4 mL DMF and sonicated. The mixture was spin-coated onto a quartz substrate at a spin speed of 500 RPM for 5 s followed by 2000 RPM for 45 s.

(ii) **Neat (for comparison)**

5 mg PyP-MOF were suspended in 2 mL MeOH, and the suspension was sonicated for 5s to allow dispersion of the MOF crystals. The dark red suspension was then drop-casted onto clean quartz substrates.

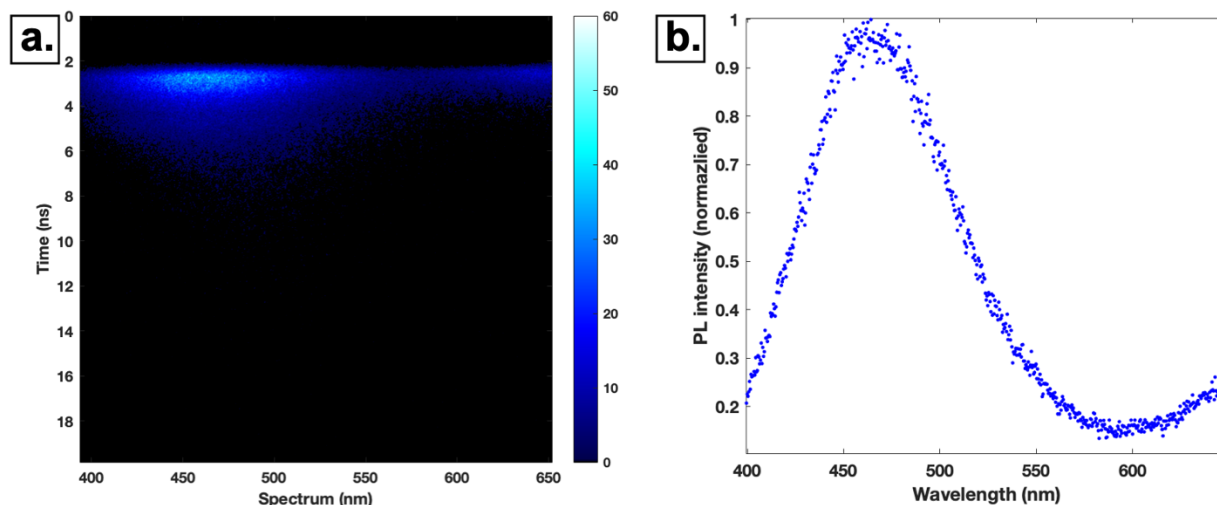


Figure S9. (a) Time-resolved spectrally resolved photoluminescence trace of PyP-MOF (diluted in polystyrene, 1 wt%). (b) Photoluminescence of PyP-MOF (diluted in polystyrene, 1 wt%) integrated over time (0-20 ns).

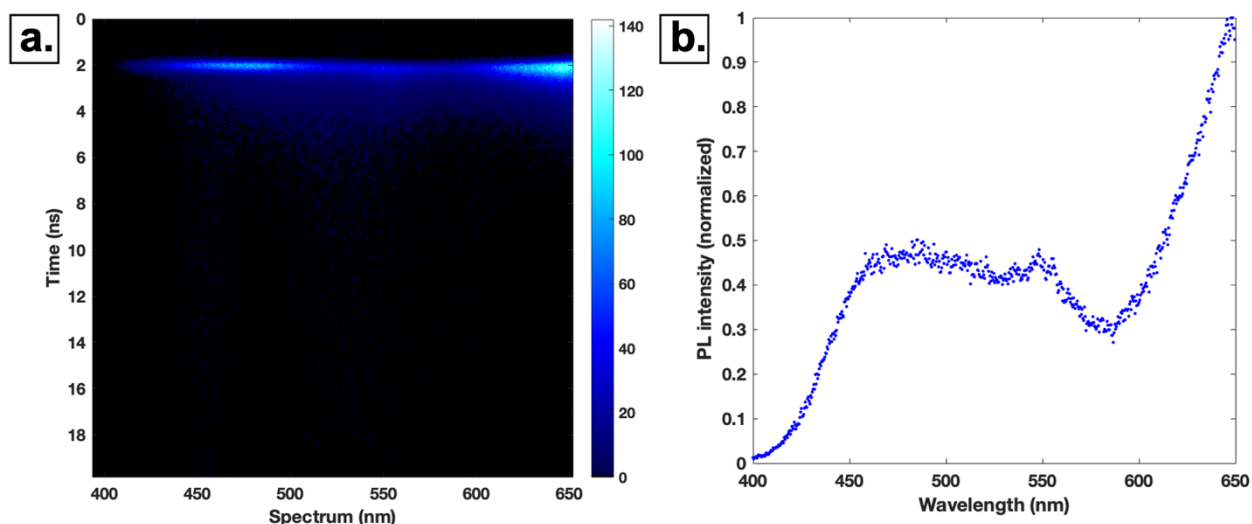


Figure S10. (a) Time-resolved spectrally resolved photoluminescence trace of **PyP-MOF** (neat, drop-casted). (b) Photoluminescence of **PyP-MOF** (neat, drop-casted) integrated over 0-20 ns.

7.3 Control Sample: Donor-Acceptor Solid Mixture (H_4TBAPy and H_2P Diluted in Polystyrene)

Sample preparation

6 mg H_4TBAPy , 6 mg H_2P and 200 mg polystyrene were dissolved in 4 mL DMF. The mixture was sonicated until the solids dissolved completely. The resulting solution was then spin-coated onto a clean quartz substrate at a speed of 500 RPM for 5s followed by 2000 RPM for 45s.

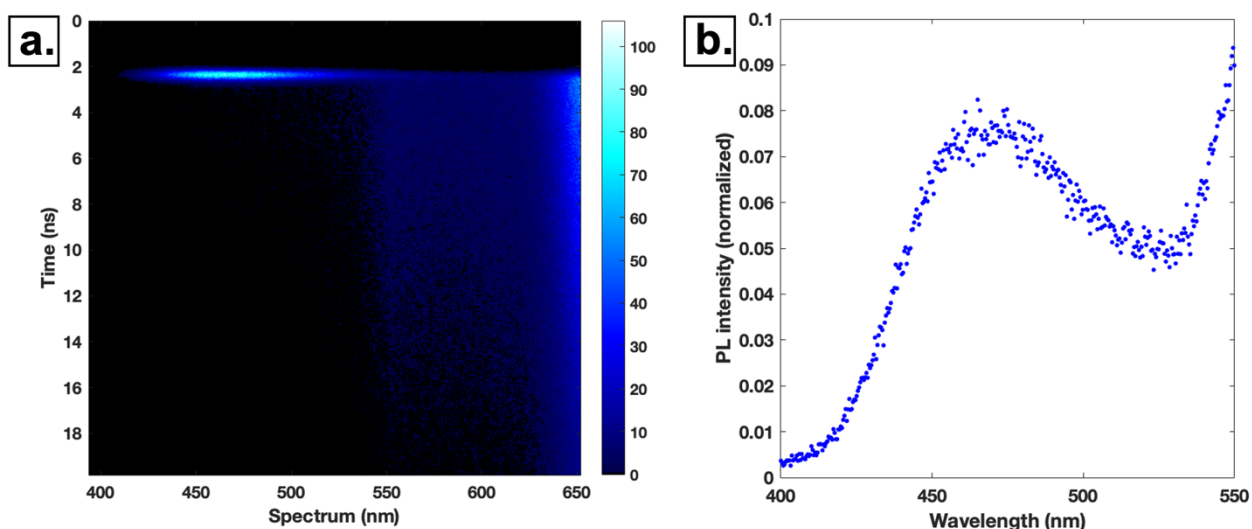


Figure S11. (a) Time-resolved spectrally resolved photoluminescence trace of donor-acceptor (D-A) mixture control sample (diluted in polystyrene, 3 wt.%). (b) Photoluminescence of D-A control sample integrated over time (20 ns).

Discussion

7.3.1 Influence of FRET efficiency on PL

Compared to the PL of the MOF samples where the FRET efficiency is low, the highly efficient FRET in the control sample significantly diminished the ratio of the donor and acceptor PL intensities ($I_{PL(D)}:I_{PL(A)}$). As shown in **Figure S9**, $I_{PL(D)}:I_{PL(A)} > 1$ for the polystyrene-incorporated MOF sample. In contrast, in control samples with much higher FRET efficiency, $I_{PL(D)}:I_{PL(A)}$ diminishes to $\ll 1$ (**Figure S11**). This is consistent with our expectation that for system with efficient FRET, the donor emission will be quenched due to the energy transfer to the acceptor. Due to the much more intense emission from the **H₂P** acceptor relative to the **H₄TBAPy** donor in the control sample, the “tail” of the acceptor emission can interfere with the calculation of the donor lifetime, if the entire donor emission spectral range were to be used for integration. Therefore, only the blue-end (400 nm-450 nm) of the **H₄TBAPy** PL is integrated for determination of the **H₄TBAPy** lifetime in the control sample to be ~ 0.08 ns (**Figure 4c**).

7.3.2 Concentration dependence of control experiment

It is worth noting that upon increasing the concentration of the control sample from 1 wt% to 3 wt% (weight percent based on the weight of **H₄TBAPy** donor relative to polystyrene), the lifetime of **S1_D** was observed to shorten from ~ 0.56 ns to ~ 0.08 ns, as shown in **Figure S12** below. In **ESI Section 7.1**, we have demonstrated that increasing the concentration of the **H₄TBAPy** donor alone does not lead to the shortening of its lifetime (**Figure S8**). Further, the **H₄TBAPy** lifetime does not show any significant variation below 8 wt%. Since the concentrations of the control samples falls within this range, the shortening of lifetime can be attributed to increased energy transfer efficiency when the donor and acceptor are brought to closer proximity in samples of higher concentration. Further increasing the concentration of control sample (i.e. decreasing the DA distance) can potential lead to higher FRET efficiency than the 96% observed for the 3 wt% sample. This further suggests that sufficient spectral overlap is present for the **H₄TBAPy** / **H₂P** pair to allow efficient singlet energy transfer.

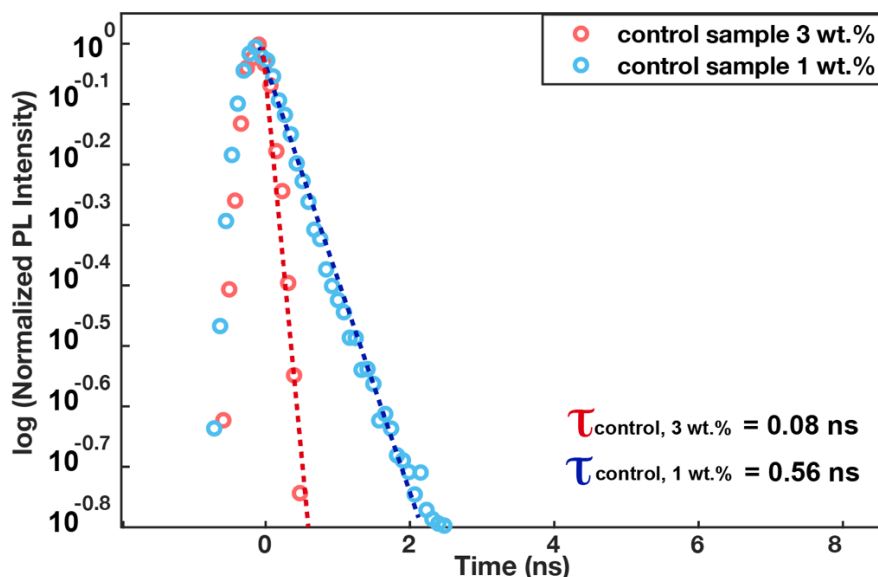


Figure S12. Comparison of the decay dynamics of control samples of two different concentrations: 3 wt% and 1 wt% (by the weight of the **H₄TBAPy** donor in polystyrene matrix).

In addition, the observed dependence of the donor's decay dynamics on the concentration of the control sample also suggests that in the control sample, the donor and acceptor moieties are well-dispersed, and we have certain level of control over the donor-acceptor separation in the control sample. This likely results from the long-time sonication of the mixture, as well as the immediate spin-coating that followed the sonication. We further performed calculation to estimate the average distance of the D and A molecules in polystyrene of the concentrated (3 wt%) control sample to be ~2.6 nm (detailed calculation presented below). This distance is larger than the D-A separation of ~1.3 nm in the **PyP-MOF** (suggested by crystallography). In addition, for the 1 wt% sample, an even larger D-A separation (~3.8 nm) can be calculated, yet it still showed more efficient energy transfer (~69%) than that of the MOF sample (< 36%). Based on these considerations, we believe that the possibility of the more efficient energy transfer of the control sample being due to shorter D-A distance is unlikely.

Detailed calculation for estimating the average D-A distance in the concentrated control sample (3 wt% of donor relative to polystyrene):

Molarity of donor (D), acceptor (A), polystyrene (PS) in the DMF solution prior to spin-coating:

$$M(A) = M(D) = \left(\frac{6 \text{ mg}}{682.68 \frac{\text{g}}{\text{mol}}}\right) / 4 \text{ mL} = 2.197 \text{ mM}$$

$$M(PS) = \left(\frac{200 \text{ mg}}{400,000 \frac{\text{g}}{\text{mol}}}\right) / 4 \text{ mL} = 0.125 \text{ mM}$$

$$\frac{M(D)}{M(PS)} \approx 17.58$$

Approximating polystyrene (PS) thin film density as 1.05 g/cm³, then in 1 cm³ thin film, the molar amount of PS =

$$\left(\frac{1.05 \text{ g}}{400,000 \frac{\text{g}}{\text{mol}}}\right) = (2.625) \cdot 10^{-6} \text{ mol}$$

Assuming the molar ratio of D, A and PS does not change upon spin-coating, then the number of D and A molecules in 1 cm³ of PS thin film are:

$$N(D) = N(A) = [(2.625) \cdot 10^6 \text{ mol}] \cdot (17.58) \cdot N_A \approx (2.78) \cdot 10^{19} \text{ molecules}$$

Assuming D and A occupy a uniform square lattice, then along each 1 cm side of the lattice, there arranges

$$\sqrt[3]{(2.78) \cdot 10^{19} + (2.78) \cdot 10^{19}} = (3.816) \cdot 10^6 \text{ D-A molecules}$$

Therefore, the distance between two neighboring D-A molecule is approximately:

$$d_{DA} = \frac{1}{(3.816) \cdot 10^6 \text{ cm}^{-1}} \approx 2.6 \cdot 10^{-7} = \mathbf{2.6 \text{ nm}}$$

which is larger than the D-A distance in the MOF (~ 1.3 nm).

7.3.3 Notes on the measurement time window

We would like to make a note on the measurement time window. Since time range is known to impact the time resolution for streak cameras, faster decaying species need to be measured in a smaller time window. Therefore, we measured the **S1_D** state for the control sample, which has a much shorter lifetime, under a shorter time window (5ns) than what's used for the **H₄TBAPy** donor-only sample or the **PyP-MOF** sample (20ns), in order to ensure the accuracy of the measured lifetime of 0.08 ns. However, for the comparison of decay curves of these three samples in the manuscript Figure 5, all data presented were taken under the 20 ns time window for the sake of keeping the comparison to a single variable.

Section 8. Photoluminescence Quantum Yield Raw Data and Discussion

8.1 PyP-MOF

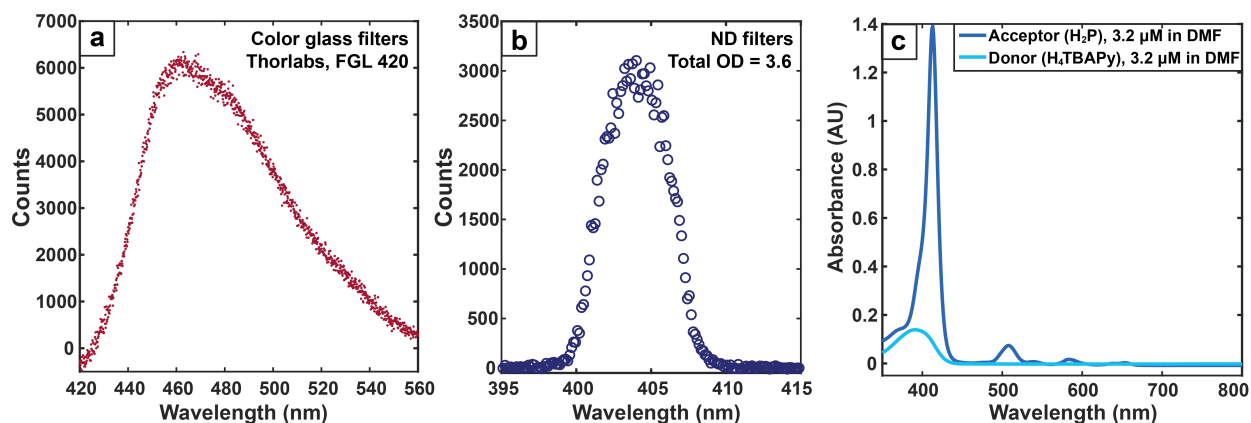


Figure S13. Spectra measured in an integrating sphere for (a) the emission and (b) the excitation regions of the photoluminescence quantum yield experiment on **PyP-MOF** (DMF suspension). Please note that the excitation signal is attenuated by absorption from both the donor and the acceptor moieties within the MOF. The approximate fraction absorbed by the donor is 13%, as estimated from (c) the absorbance of the D and A molecules at the same molar concentration (3.2 μM in DMF). The ratio of the integrated emission and excitation signals after applying correction from filters, detector and absorption fraction yields a photoluminescence quantum yield of $\sim 6.8\%$.

The PLQY measurement of **PyP-MOF** was performed in DMF since suspension sample increases the number of absorbed and emitted photons, thereby allowing these values to be determined more reliably. However, we observed that applying suspension samples also introduce a *concentration-dependence* to the measurement result, which originate largely from emission self-absorption.¹⁰ Since the donor and acceptor moieties within the MOF have good spectral overlap, such re-absorption effect is particularly pronounced in this material. Upon dilution of the suspension, we observed an increase of the measured PLQY up to 6.8%. Further dilution of the sample yields unreliable data due to hitting the detection limit for the absolute number of absorbed photons. Regarding the QY calculation, it is also worth noting that the number of absorbed photons directly measured contains both photons absorbed by the donor *and by the acceptor*. The percentage of photons absorbed by the donor was estimated by measuring the ratio of the molar absorption coefficients of the two moieties (Figure S13-c).

8.2 Additional discussion on the presence of other non-radiative pathways

When analyzing donor emission in both lifetime and PLQY studies, the Förster transfer to acceptor falls into the category of *non-radiative* recombination pathways. To avoid ambiguity, we'll define k_{nr} as non-radiative processes other than FRET, and k_r as the fundamental depopulating rate of the S1_D state of the pyrene-based fluorophore by light emission. Therefore,

$$k_{obs} = k_r + k_{nr} + k_{FRET}$$

$$\eta_{FRET} = \frac{k_{FRET}}{k_{r_DA} + k_{nr_DA} + k_{FRET}}$$

The value calculated from the change of lifetime can be expressed as:

$$1 - \frac{\tau_{DA}}{\tau_D} = 1 - \frac{k_{obs_D}}{k_{obs_DA}} = \frac{(k_{r_DA} - k_{r_D}) + (k_{nr_DA} - k_{nr_D}) + k_{FRET}}{k_{r_DA} + k_{nr_DA} + k_{FRET}} = \eta_{FRET} + \frac{k_{nr_DA} - k_{nr_D}}{k_{obs_DA}}$$

(Note: k_r is less likely to experience significant influence from the environment, but we acknowledge that effects such as interaction with plasmonic surfaces and photonic microcavities can induce changes in k_r .)

$$\therefore \eta_{FRET_DA} = \left(1 - \frac{\tau_{DA}}{\tau_D}\right) - \frac{(k_{nr_DA} - k_{nr_D})}{k_{obs_DA}}$$

$$\text{Defining } \frac{(k_{nr_DA} - k_{nr_D})}{k_{obs_DA}} \equiv \delta_{nr}, \text{ then } \eta_{FRET_DA} = \left(1 - \frac{\tau_{DA}}{\tau_D}\right) - \delta_{nr} \quad (\text{Eq. 1})$$

As expressed here, the correction term δ_{nr} accounts for differences in *non-FRET* nonradiative recombination pathways between the donor-acceptor structure and the donor-only sample used as a reference. Assigning $\delta_{nr} = 0$, as is routinely done in the literature, makes the implicit assumption that all of the observed difference in the lifetime of the donor can be assigned to energy transfer.

As brought up in the main manuscript, it has previously been suggested in literature that additional non-radiative pathways can arise upon anchoring the H₄TBAPy fluorophore into MOF structures.¹¹ To test this, we carried out PLQY comparisons in additional control systems. We measured the PLQY of a MOF consisting of *only* the H₄TBAPy donor (NU901) to be 7.7 %, which is partially quenched in comparison to that of H₄TBAPy molecule diluted in spin-coated polystyrene thin films (17 %). Since the quantum yield of the H₄TBAPy fluorophore is known to be influenced by solvent interaction, we measured the aforementioned PLQY of NU901 and H₄TBAPy both as solvent-free films to avoid changing other variables. Thus, the result of this comparison is consistent with literature insight that additional non-radiative pathways can be introduced upon MOF-incorporation for H₄TBAPy. We speculate that framework vibration could contribute to such non-radiative pathways.

Bringing this observation into the context of the **PyP-MOF**, we infer that for this D-A system \subset MOF,

$$(k_{nr_DA} - k_{nr_D}) > 0, \quad (\text{i. e. } \delta_{nr} > 0)$$

Thus by Eq. 1 and data we reported the manuscript,

$$\eta_{FRET} < \left(1 - \frac{\tau_{DA}}{\tau_D}\right) = 36\%$$

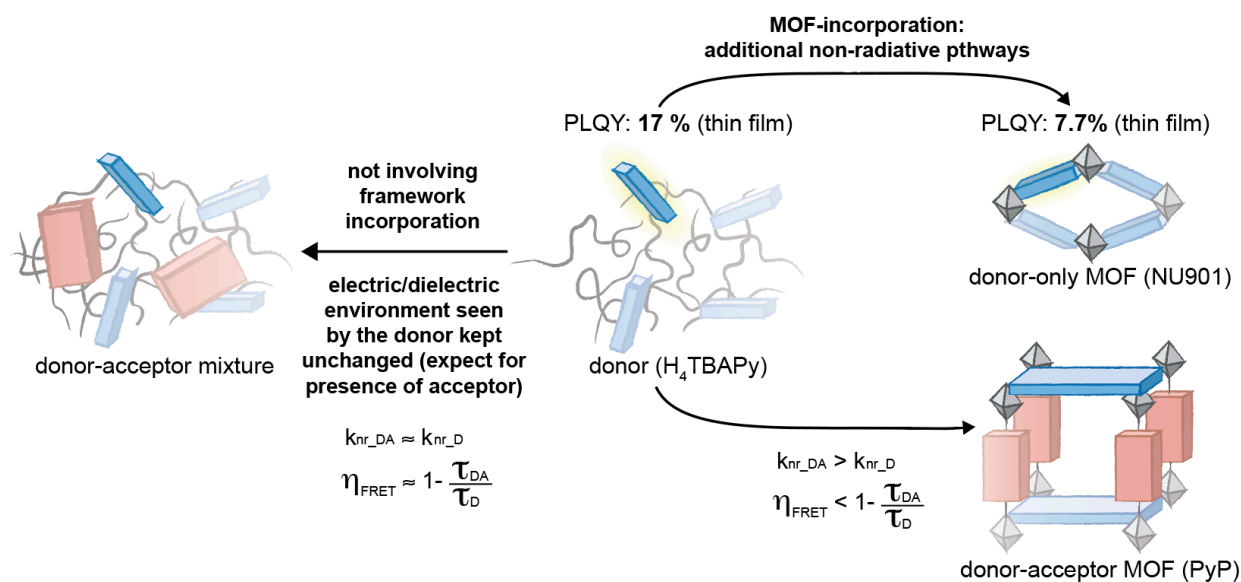


Figure S14. Comparison of changes in additional non-radiative pathways in situations with (right) and without (left) framework-incorporation.

On the other hand, such framework-induced non-radiative pathways are not involved in the D-A solid mixture. In this case, all factors that could influence the electric and dielectric environment experienced by the donor are kept identical to those of the donor-only sample (except for the introduction of an acceptor). Therefore, for the donor-acceptor mixture, $k_{nr_DA} \approx k_{nr_D}$, $\eta_{FRET} \approx (1 - \tau_{DA}/\tau_D) = 96\%$, supporting the validity of our claim that our chosen donor and acceptor bear sufficient spectral overlap to allow efficient energy transfer.

To further test this claim, we carried out PLQY comparisons on an additional set of control system: donor-acceptor mixtures in DMF solution. As shown in the data in **Table S3**, the PLQY of donor-acceptor mixture solution bears a strong concentration-dependence. The increased degree of donor quenching with increasing concentration suggests that a major quenching pathway involves D-A interaction. If the donor and acceptor did not have sufficient spectral overlap to allow FRET, then such significant dependence of PLQY on concentration would not be expected.

Table S3. Concentration dependence of the H₄TBAPy PLQY in a mixture of H₄TBAPy and H₂P (DMF solution).

Concentration (in DMF)	3.0 mM	1.5 mM	0.75 mM	0.37 mM
PLQY (donor emission)	13%	19%	25%	31%

note: the PLQY of donor-only solution in DMF was measured to be ~68%

As discussed in the manuscript, the purpose of the control experiment is to demonstrate that our chosen donor-acceptor pair bears sufficient spectral overlap to allow D→A energy transfer. Based on combinations of (i) lifetime measurements (ii) PLQY comparison and (iii) direct demonstration of spectral overlap with absorption/emission energy level characterization (**ESI Section 6**), we conclude that this chosen D-A pair indeed allows D→A energy transfer.

Section 9. TD-DFT Calculations

Method Geometry optimization was carried out with B3LYP/def2-SVP. TD-DFT was performed at a level of CAM-B3LYP/def2-TZVP for 40 roots with CPCM (modeled with implicit solvation for benzene).

The calculation yielded frontier orbitals of the donor and acceptor moieties as below:

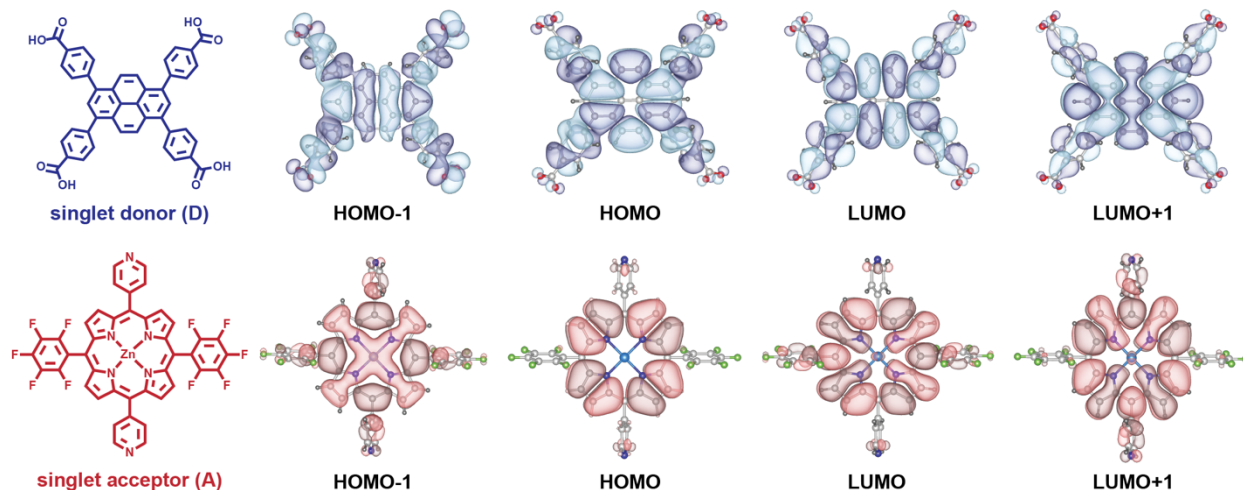


Figure S15. Summary of the calculated frontier orbitals for the donor and acceptor moieties. Isosurface levels for molecular orbital diagrams shown at 0.01.

For the pyrene-based donor moiety (calculated as tetra-anion), the transition dipoles corresponding to the main excited states are summarized in **Table S4** below. The calculation corroborates that all major transition dipole moments lie within the π -plane of the pyrene core (which in turn lies within the crystallographic ac -plane). These results are consistent with calculations of the transition dipoles of the pyrene core molecule reported in literature,¹² based on which the assignment of the 1L_a , 1L_b bands can be made.

The porphyrin chromophore is known to be a circular oscillator with two nearly degenerate, orthogonal transition moments of approximately the same magnitude,¹⁴ which is consistent with our calculation shown in the **Table S5** below. This complex nature of the porphyrin transition dipoles has led to the development of an “*Effective Transition Dipoles Model*” that is often applied to the analysis of energy transfer involving porphyrin moieties.^{14,15}

Based on this model, for porphyrin moiety with a rotational axis, the direction of its “effective transition dipole” can be approximated to lie along the direction of this rotational axis. Applying this model to our system, where the **Zn(II)-P** bears a rotational axis along the pillaring axis, we can model the effective transition dipole of **Zn(II)-P** to lie along this pillaring axis (which is parallel to the crystallographic b -axis).

Since refinement of diffraction data (both synchrotron diffraction and 3D rotational electron diffraction) suggests that the crystallographic *b*-axis is perpendicular to the crystallographic *ac*-plane (**Figure 3**), we rationalize that the transition dipoles most relevant to the singlet energy transfer between the donor and acceptor moieties are perpendicular to each other.

Table S4. Summary of the excited states calculated for the pyrene-based donor moiety (calculated as tetra-anion). Assignment of the 1L_a and 1L_b bands are made based on calculations of the pyrene core molecule reported in literature.¹²

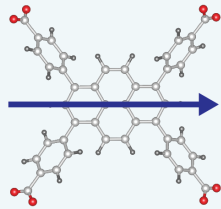
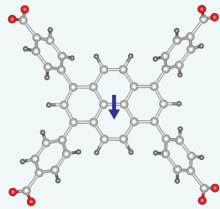
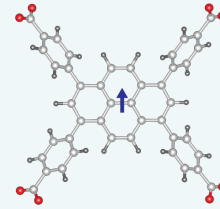
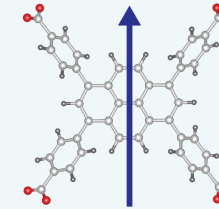
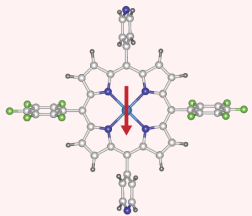
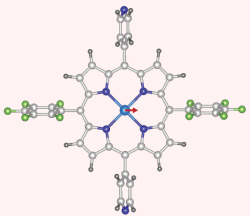
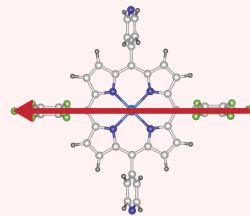
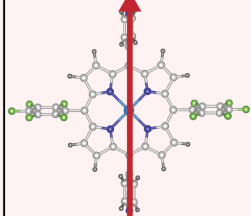
H ₄ TBAPy	STATE 1	STATE 2	STATE 3	STATE 4
Energy (cm ⁻¹)	27120.5	29925.9	34703.6	36538.6
Wavelength (nm)	368.7	334.2	288.2	273.7
Main Configuration (sign of coefficient)	HOMO → LUMO (93%, +)	HOMO → LUMO+1 (93%, +) HOMO-1 → LUMO (23%, +)	HOMO → LUMO+3 (67%, -) HOMO-1 → LUMO+5 (12%, -)	HOMO-1 → LUMO (46%, +) HOMO → LUMO+1 (30%, -)
Transition Dipole				
f _{osc}	1.500229193	0.003293074	0.004081176	2.003503765
Band	1L_a	1L_b		1L_b

Table S5. Summary of the excited states calculated for the Zn(II)-P acceptor moiety. The calculation method was selected by referencing TD-DFT calculation for porphyrins reported in literature.¹³

Zn(II)-P	STATE 1	STATE 2	STATE 3	STATE 4
Energy (cm ⁻¹)	19148.6	19162.9	28574.0	28626.1
Wavelength (nm)	522.2	521.8	350.0	349.3
Main Configuration (sign of coefficient)	HOMO-1 → LUMO+1 (42%, +) HOMO → LUMO (55%, +)	HOMO-1 → LUMO (50%, +) HOMO → LUMO+1 (48%, -)	HOMO-1 → LUMO (43%, -) HOMO → LUMO+1 (47%, -)	HOMO-1 → LUMO+1 (51%, +) HOMO → LUMO (40%, -)
Transition Dipole				
f _{osc}	0.016141341	0.000819075	2.947631415	2.967429240
Band	Qy	Qx	Bx	By

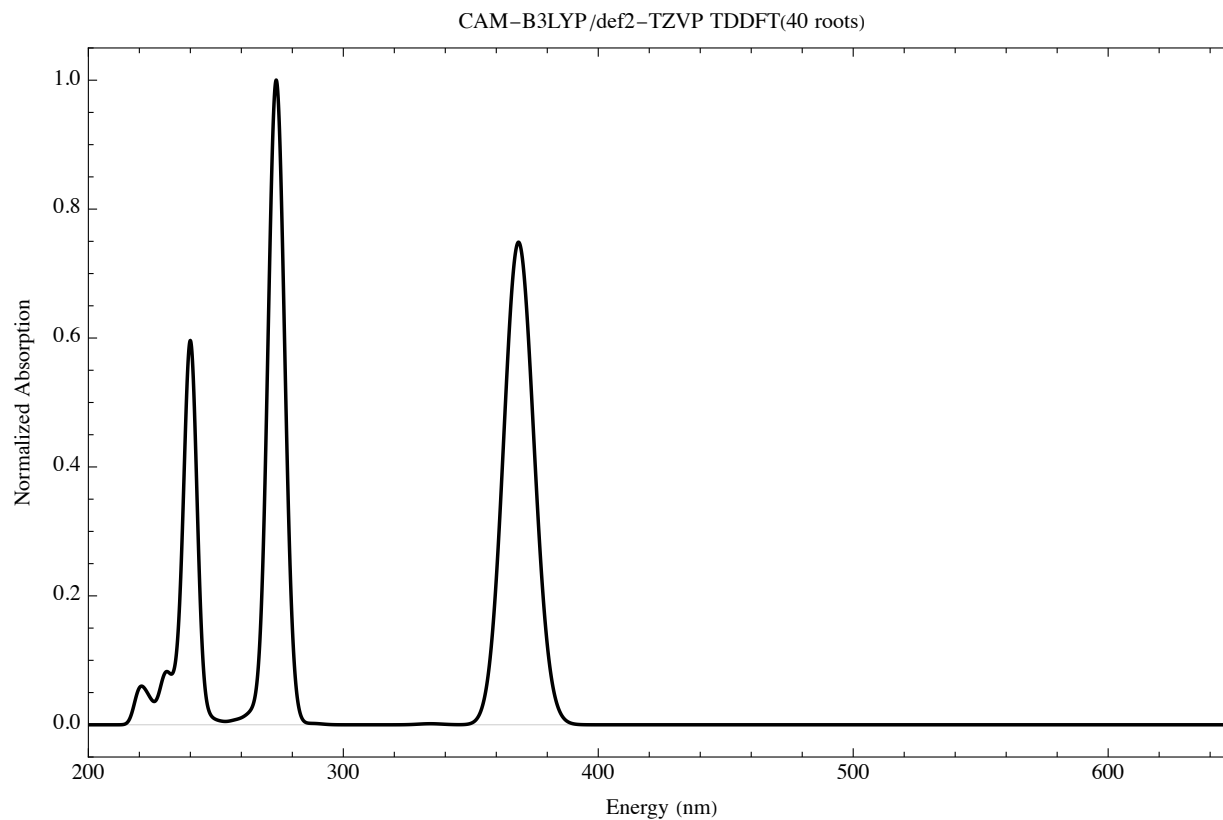


Figure S16. Calculated absorption spectrum via transition electric dipole moments for the pyrene-based donor moiety (calculated as tetra-anion). Modeled with implicit solvation for benzene, with simulated full-width half-maximum of 1000 cm^{-1} .

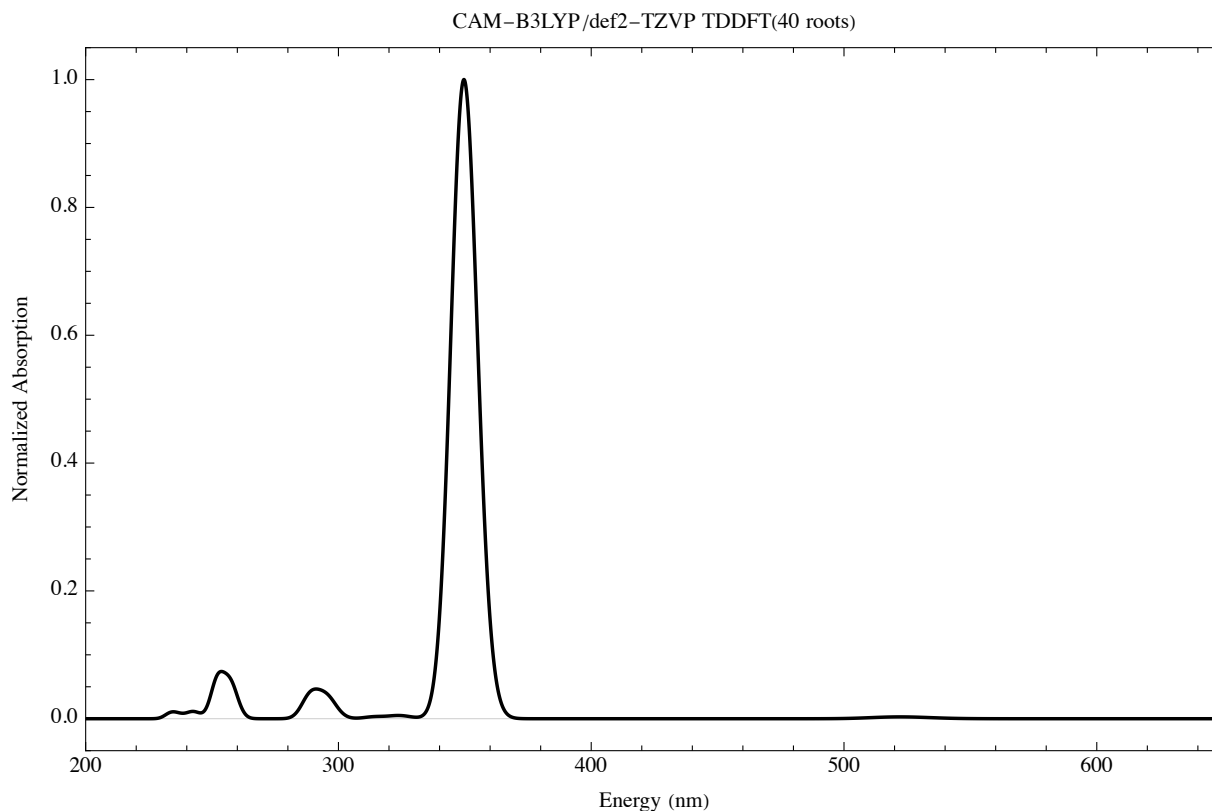


Figure S17. Calculated absorption spectrum via transition electric dipole moments for **Zn(II)-P** acceptor moiety. Modeled with implicit solvation for benzene, with simulated full-width half-maximum of 1000 cm^{-1} .

Section 10. References

- (1) Son, H.-J. *et al.* "Light-Harvesting and Ultrafast Energy Migration in Porphyrin-Based Metal–Organic Frameworks." *J. Am. Chem. Soc.* **2013**, *135* (2), 862–869.
- (2) Wang, T. C.; Vermeulen, N. A.; Kim, I. S.; Martinson, A. B. F.; J Fraser Stoddart, J. F.; Hupp, J. T.; Farha, O. K. "Scalable synthesis and post-modification of a mesoporous metal-organic framework called NU-1000" *Nat. Protocols*, **2016**, *11*, 149–162.
- (3) Dou, J.-H. *et al.* "Atomically precise single-crystal structures of electrically conducting 2D metal–organic frameworks" *Nat. Mat.* **2021**, *20*, 222–228.
- (4) Wang, J.; Toby, B. H.; Lee, P. L.; Ribaud, L.; Antao, S. M.; Kurtz, C.; Ramanathan, M.; Von Dreele, R. B. and Beno, M. A. "A Dedicated Powder Diffraction Beamline at the Advanced Photon Source: Commissioning and Early Operational Results" *Rev. Sci. Instrum.* **2008**, *79*, 085105.

- (5) Lee, P. L.; Shu, D.; Ramanathan, M.; Preissner, C.; Wang, J.; Beno, M. A.; Von Dreele, R. B.; Ribaud, L.; Kurtz, C.; Antao, S. M.; Jiao, X. “A twelve-analyzer Detector System for High-resolution Powder Diffraction” *J. Synchrotron Radiat.* **2008**, *15*, 427–432.
- (6) Shu, D.; Maser, J.; Holt, M.; Winarski, R.; Preissner, C.; Lai, B.; Vogt, S. and Stephenson, G. B. “A Robot-based Detector Manipulator System for a Hard X-ray Nanoprobe Instrument. Nucl. Instruments Methods” *Phys. Res. Sect. A Accel. Spectrometers, Detect. Assoc. Equip.* **2007**, *582*, 159–161.
- (7) Dalesio, L. R.; Hill, J. O.; Kraimer, M.; Lewis, S.; Murray, D.; Hunt, S.; Watson, W.; Clausen, M.; Dalesio, J. The Experimental Physics and Industrial Control System Architecture: Past, Present, and Future. *Nucl. Instruments Methods Phys. Res. Sect. A Accel. Spectrometers, Detect. Assoc. Equip.* **1994**, *352*, 179–184.
- (8) Valenta, J. Determination of Absolute Quantum Yields of Luminescing Nanomaterials over a Broad Spectral Range: From the Integrating Sphere Theory to the Correct Methodology. *Nanosci. Methods* **2014**, *3*, 11–27.
- (9) Gouterman, M. Optical Spectra and Electronic Structure of Porphyrins and Related Rings. In *The Porphyrins*; Dolphin, D., Ed.; Academic Press: New York, **1978**; *Vol. III, Part A*, 1–165.
- (10) Boccolini, A.; Marques-Hueso, J.; Richards, B. S. Self-absorption in upconverter luminescent layers: Impact on quantum yield measurements and on designing optimized photovoltaic devices. *Opt. Lett.* **2014**, *39*, 2904–2907.
- (11) Yu, J.; Park, J.-H.; Van Wyk, A.; Rumbles, G.; Deria, P. Excited-State Electronic Properties in Zr-Based Metal–Organic Frameworks as a Function of a Topological Network. *J. Am. Chem. Soc.* **2018**, *140*, 10488–10496.
- (12) Roos, M. K.; Reiter, S.; de Vivie-Riedle, R. Ultrafast relaxation from 1L_a to 1L_b in pyrene: a theoretical study. *Chem. Phys.* **2018**, *515*, 586–595.
- (13) Zhu, Y.; Zhou, S.; Kan, Y.; Su, Z. Electronic structures and spectra of porphyrin with fused benzoheterocycles: DFT and TDDFT-PCM investigations. **2007**, *107* (7), 1614–1623.
- (14) Matile, S.; Berova, N.; Nakanishi, K.; Fleischhauer, J.; Wood, R. W. Structural Studies by Exciton Coupled Circular Dichroism over a Large Distance: Porphyrin Derivatives of Steroids, Dimeric Steroids, and Brevetoxin B.L. *J. Am. Chem. Soc.*, **1996**, *118* (22), 5198–5206.
- (15) Pescitelli, G.; Gabriel, S.; Wang, Y.; Fleischhauer, J.; Woody, R. W.; Berova, N. Theoretical Analysis of the Porphyrin-Porphyrin Exciton Interaction in Circular Dichroism Spectra of Dimeric Tetraarylporphyrins. *J. Am. Chem. Soc.*, **2003**, *125*, 7613–7628.